Title

Enhancing the Reversibility of Lattice Oxygen Redox Through Modulated Transition Metal-Oxygen Covalency for Layered Battery Electrodes.

Journal

Advanced materials (Deerfield Beach, Fla.), 34(20)

ISSN

0935-9648

Authors

Cheng, Chen
Chen, Chi
Chu, Shiyong
et al.

Publication Date

2022-05-01

DOI

10.1002/adma.202201152

Enhancing the Reversibility of Lattice Oxygen Redox Through Modulated Transition Metal-Oxygen Covalency for Layered Battery Electrodes

Chen Cheng,[1] Chi Chen,[2] Shiyong Chu,[3] Tianran Yan,[1] Haolv Hu,[1] Xiao Xia,[1] Xuefei Feng,[4] Jinghua Guo,[4] Dan Sun,[2] Jinpeng Wu,[5,*] Shaohua Guo,[3,*] and Liang Zhang[1,*]

1. Institute of Functional Nano & Soft Materials (FUNSOM), Jiangsu Key Laboratory for Carbon-Based Functional Materials & Devices, Joint International Research Laboratory of Carbon-Based Functional Materials and Devices, Soochow University, 199 Ren'ai Road, Suzhou 215123, China
2. CAS Key Laboratory of Design and Assembly of Functional Nanostructures, Fujian Key Laboratory of Nanomaterials, Fujian Institute of Research on the Structure of Matter, Chinese Academy of Sciences, Fuzhou 350002, China
3. College of Engineering and Applied Sciences, National Laboratory of Solid State Microstructures, Collaborative Innovation Center of Advanced Microstructures, and Jiangsu Key Laboratory of Artificial Functional Materials, Nanjing University, Nanjing 210093, China.
4. Advanced Light Source, Lawrence Berkeley National Laboratory, Berkeley, CA 94720, USA
5. Department of Electrical Engineering, Tsinghua University, Beijing 100084, China

*Email: liangzhang2019@suda.edu.cn (Liang Zhang); shguo@nju.edu.cn (Shaohua Guo); jinpengwu@tsinghua.edu.cn (Jinpeng Wu)

Abstract

Utilizing reversible lattice oxygen redox (OR) in battery electrodes is an essential strategy to overcome the capacity limitation set by conventional transition metal redox. However, lattice OR reactions are often accompanied with irreversible oxygen oxidation, leading to local structural transformations and voltage/capacity fading. Herein, we propose that the reversibility of lattice OR can be remarkably improved through modulating transition metal-oxygen covalency for layered electrode of Na-ion batteries. By developing a novel layered P2-$Na_{0.6}Mg_{0.15}Mn_{0.7}Cu_{0.15}O_2$ electrode, we demonstrate that the highly electronegative Cu dopants could improve the lattice OR reversibility to 95% compared to 73% for Cu-free counterpart, as directly quantified through high-efficiency mapping of resonant inelastic X-ray scattering. Crucially, the large energetic overlap between Cu 3d and O 2p states dictates the rigidity of oxygen framework, which effectively mitigates the structural distortion of local oxygen environment upon (de)sodiation and leads to the enhanced lattice OR reversibility. The electrode also exhibits a completely solid solution reaction with the smallest volume change of 0.45% ever reported and a reversible metal migration upon cycling, which together ensure the improved electrochemical performance. Our results emphasize the critical role of transition metal-oxygen covalency for enhancing the reversibility of lattice OR toward high-capacity electrodes employing OR chemistry.

Keywords: Na-ion batteries; Layered electrodes; Lattice oxygen redox; Metal-oxygen covalency; RIXS; Structural stability

Introduction

The pressing demand for high-energy-density rechargeable batteries has stimulated enormous research efforts to pursue both conceptual breakthroughs and fundamental developments of cathode materials.[1] Conventionally, the specific capacities of cathode materials are provided only by cationic redox chemistry, mainly transition metal (TM) redox, which are approaching the theoretical limits and thus insufficient for the ever-increasing practical demands.[2] More recently, anionic redox chemistry, typically oxygen redox (OR), has emerged as a promising paradigm to enable more energy storage than the traditional cationic redox, leading to the enhanced power and energy densities of cathode materials.[3, 4] For example, with the synergistic cationic redox and anionic redox, Li-rich $Li_{1+x}Ni_yCo_zMn_{1-x-y-z}O_2$ cathode can achieve a high specific capacity exceeding 300 mAh/g, which far exceeds the commercial Li-ion cathode materials based solely on cationic redox.[5] However, it has been found that the OR activities for both Li- and Na-ion systems are frequently accompanied with irreversible oxygen gas release, radical oxygen evolution, and surface reactions, resulting in performance decays in both voltage fade and capacity decay. [6, 7] In the meantime, several works have clarified that some of these detrimental effects are not related to the reversible OR reactions in the bulk lattice, hereafter called "lattice OR".[8, 9] Therefore, it is critical to distinguish the lattice OR from other oxygen activities through reliable characterization techniques, and more importantly, improve the reversibility of lattice OR through rational design rules to achieve high-performance cathodes.

It has been proposed that the presence of A-O-A' local configurations in the cathode materials is the prerequisite for the activation of lattice OR activities, where A stands for Li or Na and A' represents non-redox active elements with no covalent interaction with oxygen (such as Li, Na, Mg,

Zn, Al, and Ti).[10] Such unique configurations could lead to the formation of O 2p nonbonding states just below Fermi level, which will trigger the lattice OR activities.[11-13] Although extensive studies have been reported, most of them did not clearly distinguish the difference between lattice and non-lattice OR activities.[14-16] On the other hand, the reversibility of the activated lattice OR reactions is still elusive considering the labile characteristics of the O 2p nonbonding states. For instance, the initial-cycle reversibility of lattice OR reactions of $Li_{1.17}Ni_{0.21}Co_{0.08}Mn_{0.54}O_2$ cathode with a typical Li-O-Li local configuration is only 76%, which is much lower than that of the conventional cationic redox reactions.[17] Therefore, enhancing the reversibility of lattice OR is imperative for practical applications of rechargeable batteries.

Herein, we distinguish the lattice OR and demonstrate that its reversibility can be enhanced through the modulation of transition metal (TM)-oxygen covalency for layered battery electrodes. The benchmark material we investigated in this study is P2-type layered $Na_{0.6}Mg_{0.3}Mn_{0.7}O_2$ (NMMO) for Na-ion batteries, with its stoichiometry deliberately adjusted to minimize the Mn redox during the initial charge process by increasing the nominal valence of Mn to +4. By partially substituting low-electronegativity Mg^{2+} with high-electronegativity Cu^{2+}, a novel $Na_{0.6}Mg_{0.15}Mn_{0.7}Cu_{0.15}O_2$ (NMMCO) cathode is developed, with the enhanced TM-O covalency. Based on the quantitative analysis of high-efficiency mapping of resonant inelastic X-ray scattering (mRIXS) results, it is revealed that the reversibility of lattice OR is greatly improved from 73% for NMMO to 95% for NMMCO as a consequence of Cu dopants. In addition, the undesired P2–OP4 phase transition is successfully suppressed with an ultra-low volume change of 0.45%, which is the smallest value ever reported. Moreover, owing to the highly reversible lattice OR reactions, the irreversible TM migration is also largely mitigated. Density functional theory (DFT) calculations

disclose that the large energetic overlap between Cu 3d and O 2p states ensures the rigidity of oxygen framework by effectively suppressing the structural distortion of local oxygen environment, which leads to the improved reversibility of lattice OR activities. Our work unambiguously shows the critical role of TM-O covalency for maintaining reversible lattice OR activities, which provides a novel perspective for rationally designing high-performance cathode materials with anion-cation synergetic contribution.

Results and discussion

P2-type NMMO and Cu-substituted NMMCO were synthesized through simple one-step solid-state reaction and characterized by X-ray diffraction (XRD) (Figure 1a). All diffraction peaks can be well indexed to a hexagonal P2 phase with a space group of *P*63/*mmc*. In addition, two additional superlattice peaks at 20.6° and 26.2° are observed for NMMO (Figure 1b), implying that the Mg and Mn ions are distributed with a honeycomb ordering in the TMO_2 layer.[18] Such ordering determines the electrostatic force between TM and coordinated oxygen atoms, which could greatly affect the structural stability during cycling.[19] In contrast, these superlattice peaks are not observed for NMMCO, suggesting the successful suppression of Mg/Mn ordering by Cu dopants. This could change the local environment of oxygen and thus further improve the structure stability during (de)sodiation process.

The morphological structure of NMMCO was further investigated by scanning electron microscopy (SEM) and transmission electron microscopy (TEM) (Figure 1c, d). The sample exhibits a multilayer-stacked hexagonal nanosheet structure, which may facilitate the Na-ion transport due to the increased contact area with electrolyte. The precise atomic-level structural information of NMMCO was studied by high-angle annular dark field (HAADF)-spherical

aberration corrected scanning transmission electron microscopy (STEM) (Figure 1e), which clearly demonstrates the distinct alignment of TM atoms with an interatomic distance of 0.24 nm, matching well with the d-spacing value of [001] crystallographic direction of the material. In addition, the diffraction spots in the selected-area electron diffraction (SAED) pattern (Figure 1f) are well indexed to the corresponding TM arrange along [001] direction in a typical hexagonal symmetry phase. Furthermore, the energy-dispersive spectroscopy (EDS) elementary mapping (Figure 1g-k) suggests that all the elements are evenly distributed in the NMMCO sample.

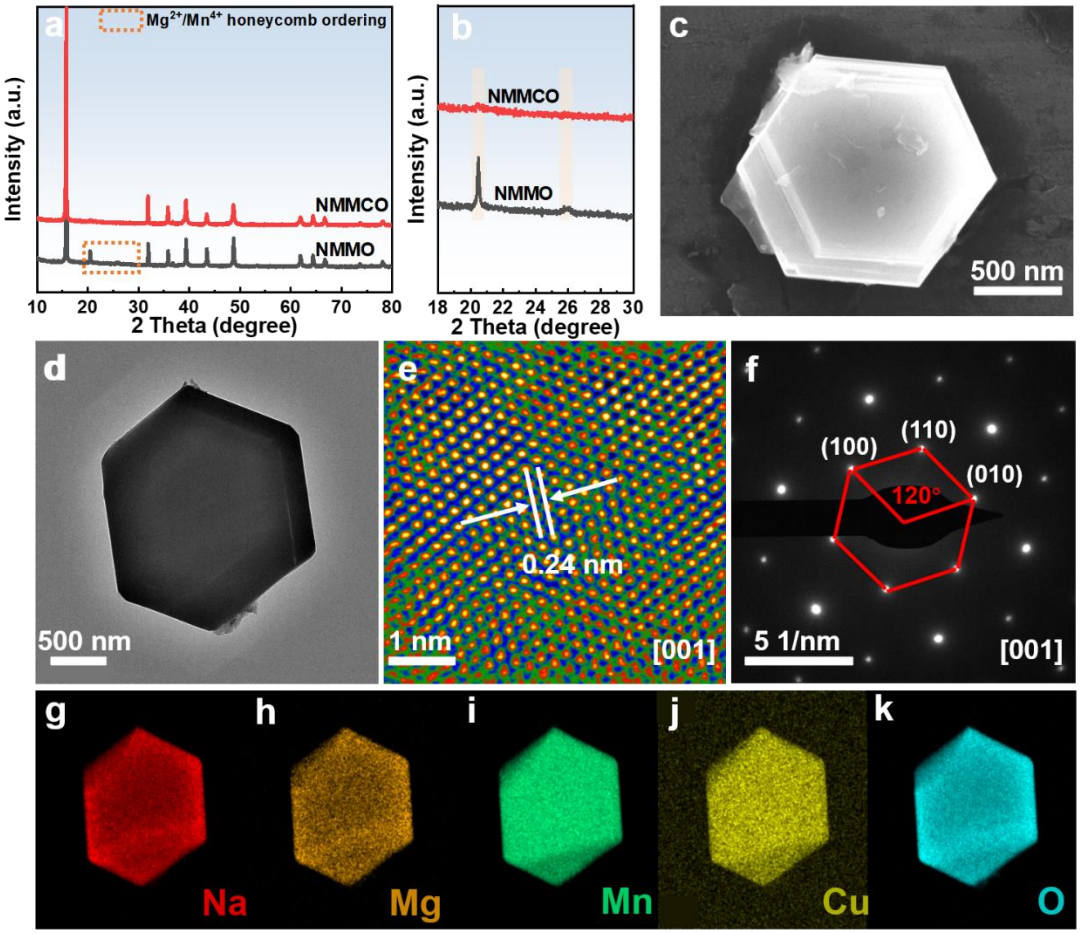

Figure 1. (a) XRD patterns of NMMO and NMMCO. (b) The zoomed-in XRD patterns. (c) SEM image, (d) TEM image, (e) HAADF-STEM image, (f) corresponding SAED image, and (g-k) EDS maps of NMMCO.

The electrochemical properties of NMMCO and NMMO were systematically investigated using

Na half cells in the voltage range of 2.0 to 4.5 V (Figure 2). The galvanostatic charge/discharge profiles of the first cycle of NMMCO and NMMO at a current rate of 0.1 C (1 C=170 mA/g) are shown in Figure 2a. For NMMO, it shows a single long 4.24 V plateau upon charging, which contributes almost the entire charge capacity. Because the nominal valence of Mn in NMMO is +4 and could not be further oxidized within layered oxide cathodes, it is inferred that the charge capacity mainly comes from the contribution of oxygen.[20] During the discharge process, the high voltage plateau does not appear but is replaced by a slope line, indicating a relatively large voltage hysteresis between charging and discharging. In contrast, the first charge process of NMMCO exhibits two stages with a slope region and a 4.38 V plateau, which should correspond to Cu^{2+} oxidation and oxygen oxidation, respectively, as discussed in details later. Interestingly, the plateau corresponding to oxygen oxidation shifts to higher voltage (4.24 vs. 4.38 V) and contributes less capacity after Cu doping, accompanied with alleviated OR voltage hysteresis, which can be better visualized in the corresponding dQ/dV curves (Figure S1). Upon discharging, a specific capacity of 157 mAh/g is achieved for NMMCO, which is much higher than that of NMMO (113.7 mAh/g). The higher discharge capacity of NMMCO should be related to Cu redox.

To better understand the kinetic difference between the redox reactions taking place at different voltages, galvanostatic intermittent titration technique (GITT) was carried out for NMMO and NMMCO (Figure 2b). It is clear that almost no voltage relaxation in the low voltage region is observed for NMMCO, indicating that the Cu redox is kinetically favorable. Moreover, the overpotential of OR reactions is considerably lower for NMMCO compared with NMMO, suggesting the enhanced redox kinetics after Cu doping. As a consequence, the rate performance of NMMCO is greatly improved (Figure 2c), with discharge capacities of 151.1, 152.1, 126.9, 106.9,

88.5, and 58.9 mAh/g at 0.1, 0.2, 0.5, 1, 2, and 5 C, respectively. Moreover, the discharge capacity is mostly recovered to its initial capacity after the current rate is set back to 0.1 C, suggesting its superior reversibility.

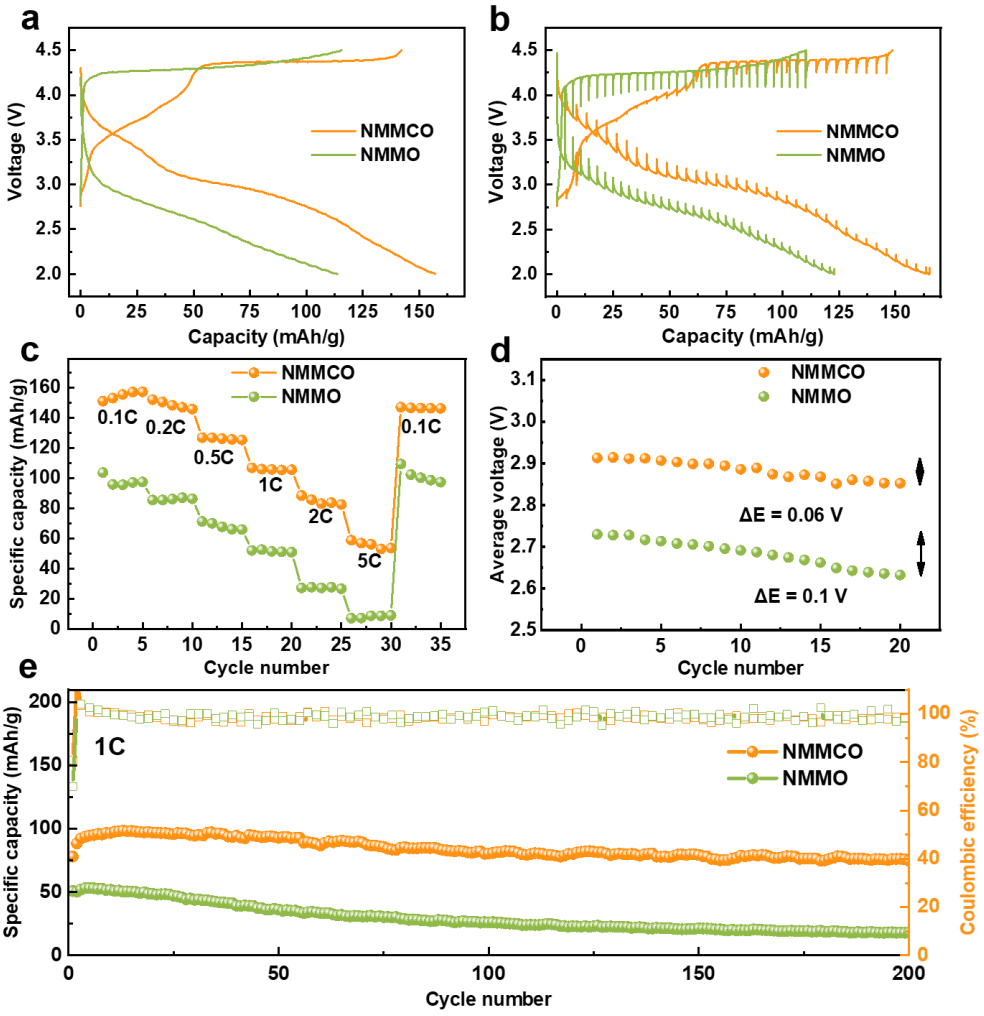

Figure 2. (a) First-cycle charge/discharge profiles of NMMO and NMMCO at a current rate of 0.1 C. (b) GITT curves. (c) Rate performance of NMMO and NMMCO. (d) Average voltage fade of NMMO and NMMCO at a current rate of 0.1 C. (e) Cycling performance of NMMO and NMMCO at a current rate of 1 C.

It should be noted that voltage fade has been frequently observed for cathode materials of Li- and Na-ion batteries, resulting in the rapid fading of delivered energy density.[21] Figure 2d shows the average voltage of NMMCO and NMMO for the first 20 cycles. It is apparent that the Cu dopants

can not only improve the average voltage but also suppress the voltage fade, leading to the enhancement and retention of energy density. More impressively, the NMMCO cathode demonstrates a greatly improved cycling stability when cycling at a high current rate of 1 C (Figure 2e), with an outstanding capacity retention of 95.8% after 200 cycles and a high Coulombic efficiency > 99%. In contrast, the NMMO cathode shows a rapid capacity decay from 50.9 mAh/g in the first cycle to 18 mAh/g after 200 cycles, which corresponds to a capacity retention of only 35.4%. Compared with previously reported P2-type electrode materials,[22-27] such as $Na_{2/3}Zn_{0.3}Mn_{0.7}O_2$,[26] $Na_{2/3}Ni_{1/3}Mn_{1/3}Ti_{1/3}O_2$,[23] $Na_{0.67}Al_{0.1}Mn_{0.9}O_2$,[24] and $Na_{0.67}Cu_{0.28}Mn_{0.72}O_2$,[25] our present study demonstrates the simultaneous improvement of specific capacity and rate capability as well as suppression of voltage fade and capacity decay through appropriate element doping.

In order to further understand the improved electrochemical performance by Cu substitution, in-situ XRD was performed to investigate the structural evolution of NMMCO upon cycling (Figure 3a). The stacking graph shows the continuous shift of main diffraction peaks without appearance of additional diffraction peaks beyond the P2 phase, indicating a completely solid-solution behavior of NMMCO in the whole voltage range. More specifically, during the charge process, the (002) and (004) peaks corresponding to the lattice parameter c consecutively shift toward lower angles while the (100) and (102) peaks related to the lattice parameters a/b monotonically shift to higher angles (Figure 3b), suggesting that the c axis is expanding and the ab plane is contracting. The expansion of c axis is attributed to the enhanced electrostatic repulsion of adjacent oxygen layers due to Na-ion extraction. In contrast, the oxidation of Cu and O during the charge process leads to shorter Cu-O distance, resulting in the shrinkage of ab plane. Moreover, these peaks evolve in completely opposite directions and eventually return to their original positions during the subsequent discharge

process. The evolution of diffraction peaks for the second cycle is the same as the first cycle (Figure 3a, b), indicating a highly reversible and sustainable structural evolution of NMMCO during charge-discharge process.

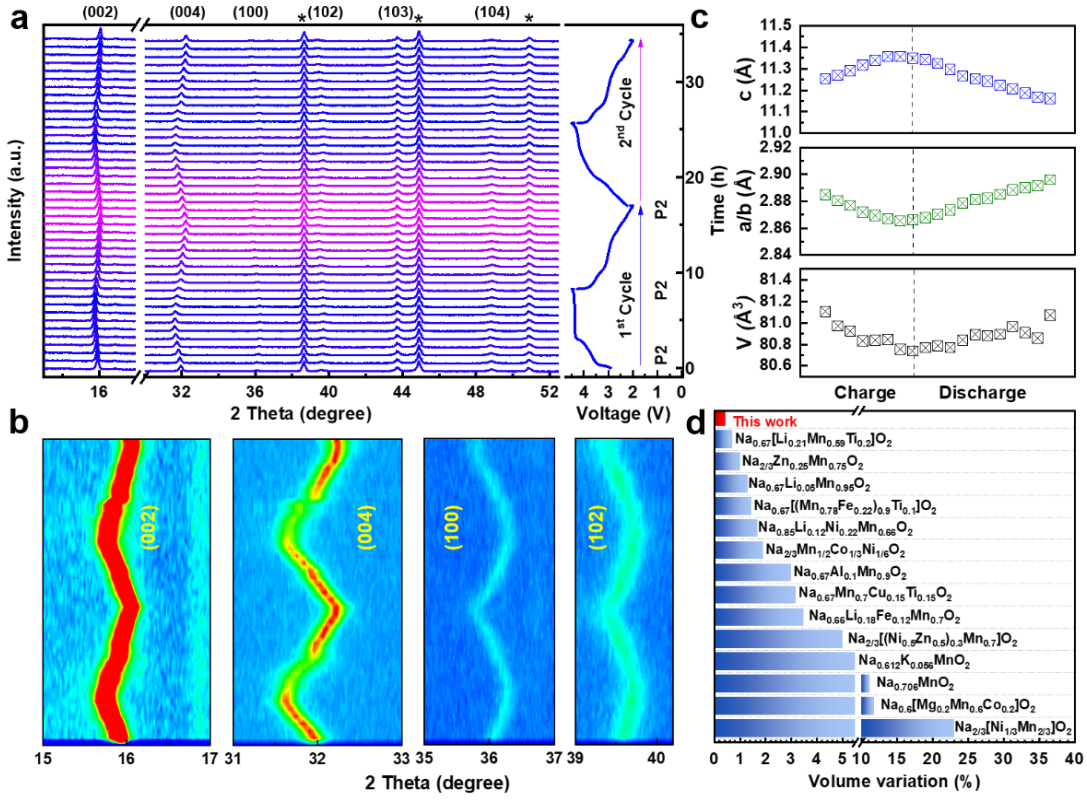

Figure 3. (a) In-situ XRD patterns of NMMCO during the initial two cycles at 0.1 C in the voltage range of 2.0–4.5 V. The asterisks represent diffraction peaks from Al current collector or Be window. (b) Corresponding contour maps of main diffraction peaks. (c) Variation of unit cell parameters a/b (green points), c (blue points), and V (black points). (d) Comparison of unit cell volume variation of NMMCO with other typical layered cathodes.

Figure 3c shows the variation of lattice parameters of NNMCO derived from the in-situ XRD results. The reversible evolution of the lattice parameters is consistent with the variation of diffraction peaks discussed above. Notably, the unit cell volume change of NMMCO before and after Na-ion extraction is merely 0.45%, which is the smallest value ever reported to the best of our

knowledge. The comparison of unit cell volume variation of NMMCO with other typical Na-ion layered cathodes is shown in Figure 3d.[22, 24, 28-38] It is worth mentioning that the large Na^+ radius could lead to large volume contraction and expansion during charge and discharge process, causing structural deterioration and capacity fading.[39] The extremely small volume variation of NMMCO reported here is close to zero-strain characteristics and should be responsible for the outstanding structural stability upon cycling.

For comparison, the structural evolution of Cu-free NMMO was also investigated by ex-situ XRD (Figure S2). Interestingly, a new diffraction peak corresponding to OP4 phase appears at ~18° at the end of first charge process, indicating the presence of common P2-OP4 phase transition that has been frequently observed for P2-type cathode materials.[40] At the end of discharge, the diffraction peaks assigned to P2 phase become asymmetric with reduced intensity. Moreover, the superlattice peak associated with metal honeycomb ordering gradually diminishes upon charging and does not reappear at the end of discharge, both indicating the inferior structural reversibility of NMMO. Such phase transition and irreversible structural evolution build up the internal strain and bring a detrimental effect on the long-term cycling stability of the cathode material.

It has been proposed that one of the main causes of phase transition is the anisotropy change of TM-O bonds during the redox reactions, which ultimately leads to the excessive glide of TMO_2 layers upon deep desodiation.[41] Herein, the partial substitution of Mg with Cu possessing similar ionic radius but distinct electronic states is expected to mitigate the anisotropy change of TM-O bonds as a consequence of strong Cu-O covalency, which should be beneficial for maintaining the stable TM-O lattice integrity.[34] Overall, the Cu dopants not only realize an absolute solid-solution behavior by suppressing the undesired phase transition but also lead to near zero-strain performance

of NMMCO cathode, which are responsible for the excellent cycling stability achieved at 1 C over 200 cycles.

To further clarify the TM redox mechanism, ex-situ X-ray absorption near-edge structure (XANES) characterizations were performed (Figure S3). The Mn K-edge XANES spectra of both NMMCO and NMMO barely change after charging to 4.5 V (Figure S3a, b), implying that tetravalent Mn is electrochemically inactive in the first charge process. Upon discharging to 2.0 V, the spectra show apparent shifts toward lower-energy region, indicative of the reduction of Mn to lower valence state. The near edges of NMMCO and NMMO recover to the initial position in the second charge process, suggesting the Mn redox is electrochemically reversible. Similarly, Cu also involves the charge compensation during the cycling process for NMMCO (Figure S3c, d), as evidenced by the Cu K-edge XANES spectra. Therefore, both Mn and Cu redox reactions are responsible for the TM charge compensation mechanism for NMMCO, in good agreement with the voltage profiles and dQ/dV results.

It has been found that the evolution of Mn valence state upon cycling is closely related to the reversibility of oxygen activities of cathode materials, with irreversible oxygen release inducing the reduction of Mn valence state and directly leading to the voltage decay.[42] Therefore, Mn L-edge soft X-ray absorption spectra (sXAS) were measured for the two cathodes at fully charged states after 1, 5, and 10 cycles (Figure S4), which could provide the most direct and quantitative detection of Mn 3d states.[43] Note that the bulk-sensitive total fluorescence yield (TFY) mode of Mn L-edge sXAS encounters serious lineshape distortions due to the self-absorption effect, impeding the reliable quantifications (Figure S5).[44] Therefore, we measured the non-distorted bulk-sensitive Mn L-edge inverse partial fluorescence yield (iPFY) spectra to quantify the valence state evolution of Mn

through the well-established linear combination fitting of the $Mn^{2+/3+/4+}$ reference spectra.[8, 9] As shown in Figure S4a, b, the fitting results (dotted lines) are in good agreement with the experimental data (solid lines), indicating an accurate quantification of the Mn valence states(Figure S4c, d and Table S1). It is apparent that the valence state of Mn in both cathodes decrease gradually with increasing cycle number. Specifically, the content of Mn^{4+} drops from nearly 100% to 91.13% for NMMO and 95.77% for NMMCO after 10 cycles, accompanied with an increased amount of Mn^{3+} to 8.87 % for NMMO and 4.23% for NMMCO, respectively. Our quantitative analysis based on Mn L-edge iPFY results clearly reveals that the overall Mn valence states drop gradually upon extended cycling, leading to the observed voltage decay. Therefore, the higher Mn valence state and thus ameliorated voltage decay of NMMCO may imply a higher reversibility of OR chemistry.

To verify this scenario, we employed the recently developed high-efficiency mRIXS to quantify the lattice OR reactions through previously demonstrated methodologies.[8, 17] Note that most of the reported endeavors to probe OR reactions were mainly based on popular O K-edge photoelectron and/or absorption spectroscopies, which are limited by the shallow detection depths (1-5 nm) and overwhelming effect of TM-O hybridization, respectively.[45, 46] In contrast, O K-edge mRIXS has been established as an effective tool to isolate the lattice OR signature from the strong TM-O hybridization features and regarded as one of the most reliable and powerful techniques to probe the lattice OR chemistry in various battery cathodes.[17, 47] Figure 4a-c and d-f display the O K-edge mRIXS images of NMMCO and NMMO at different states of charge in the first cycle, respectively. The broad features around 525 eV emission energy found in all samples originate from the TM-O hybridization states, which are split into t_{2g} and e_g states because of a combined effect of exchange energy and crystal field.[48]

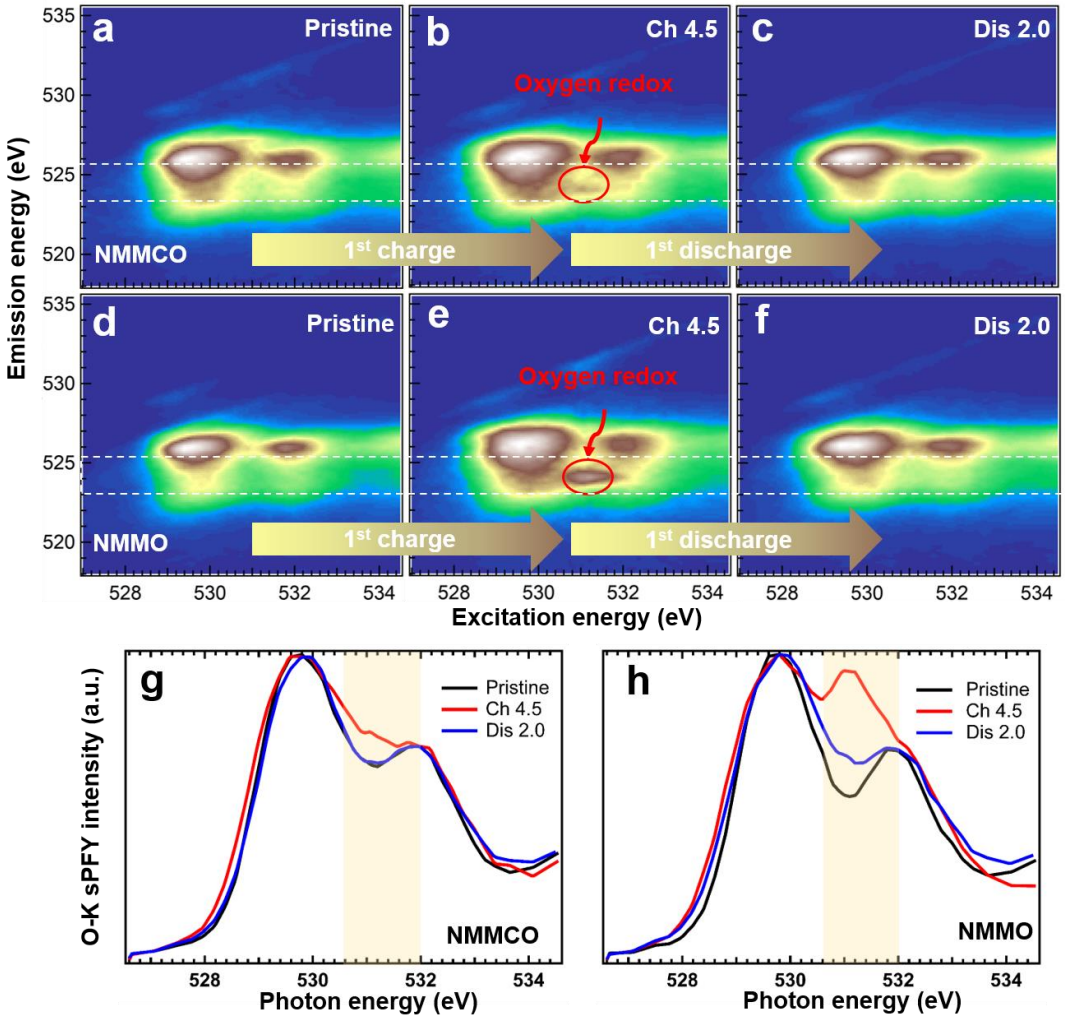

Figure 4. O K-edge mRIXS of (a-c) NMMCO and (d-f) NMMO at different states of charge of the first cycle. The red cycles indicate the oxidized lattice oxygen feature that represents the lattice OR reactions. The dashed lines on mRIXS images show the energy range for extracting the O K-edge sPFY spectra. O-K sPFY spectra of (g) NMMCO and (h) NMMO at different states of charge. The lattice OR contribution is calculated based on the sPFY intensity difference within the shaded area between different states of charge.

Strikingly, the fingerprint feature of oxidized oxygen at 531 eV excitation energy and 523.7 eV emission energy emerges at fully charged state for both NMMCO (Figure 4b) and NMMO (Figure 4e), with a lower intensity for the former. This suggests that NMMO triggers more lattice oxygen

oxidation than NMMCO, which is consistent with the longer high-voltage plateau observed in the first charge process for NMMO. These oxidized oxygen features largely disappear at fully discharged state for both NMMCO (Figure 4c) and NMMO (Figure 4f). Interestingly, the degree of lattice oxygen oxidation is negatively correlated to the electrochemical properties of the investigated cathode materials, which is contrary to the conventional wisdom.[49, 50]

Therefore, the reversibility of lattice OR reactions is quantitatively analyzed using the super partial fluorescence yield (sPFY) extracted by integrating the characteristic emission energy window around 523.7 eV (dashed lines in Figure 4a-f) in the mRIXS images. Obviously, the intensity around 531 eV excitation energy changes apparently with different electrochemical states, accompanied with the appearance of a peak and dip in fully charged and discharged state, respectively (Figure 4g and h). Correspondingly, the intensity of lattice OR feature can be quantified by integrating the sPFY area within 530.5 to 532 eV energy (shaded area in Figure 4g and h), as reported previously.[8, 17]

The quantified integration area from O K-edge sPFY of NMMCO and NMMO are summarized in Table S2. There are several important points derived from our quantification results. First, it is clear that compared to NMMCO, NMMO presents a stronger lattice oxygen oxidization in the first charge process, suggesting more lattice oxygen is electrochemically activated. Second, a remarkably high reversibility of lattice OR reactions is achieved for NMMCO (95%), which is much higher than that of NMMO (73%). Such significant contrast between NMMCO and NMMO strongly implies that Cu substitution plays a critical role to improve the reversibility of lattice OR reactions. Third, the cyclability and stability of lattice OR reactions were also investigated and compared by measuring O-K mRIXS of NMMCO and NMMO at the second fully charged state (Figure S6). An

interesting phenomenon is that the intensity of lattice OR feature of NMMCO becomes even stronger than that of NMMO, indicating the superior lattice OR capacity retention enabled by Cu doping. Fourth, the TM-O hybridization features of NMMCO (Figure S6) get broadened compared to that of NMMO because of the stronger covalency of TM-O bonds with the increase of Cu and Mn oxidation states. Based on above observations, we propose that the high reversibility and cyclability of lattice OR reactions together with the high structural stability should be responsible for the excellent electrochemical performance of NMMCO. These results also highlight the importance of enhancing the reversibility of lattice OR reactions rather than just activating the electrochemical activity of oxygen toward high-energy-density battery systems.

It has been revealed that different oxygen activities impose distinct effects on oxygen sublattice integrity and complicate the local structural environment.[6, 10, 51] For example, the irreversible OR behavior could induce irreversible "P2-O2/OP4" phase transition, leading to the rapid capacity fade.[32, 37] Also, the irreversible OR can facilitate certain local structure evolution such as atomic rearrangements and bond distortions.[52] To further elucidate the coupling relationship between structure evolution and redox behavior, we next investigated the local structure changes of NMMCO and NMMO during charge and discharge processes by extended X-ray absorption fine structure (EXAFS) quantitative analysis and electron microscopy characterization.

The Mn K-edge Fourier-transformed EXAFS (FT-EXAFS) spectra and fitting results of NMMCO and NMMO in R-space (K-space) at different electrochemical states are demonstrated in Figure 5a, b (Figure S7, 8), respectively. The experimental results overlap very well with the fitting curves, indicating the highly reliable EXAFS fitting results. The structural parameters derived from the fitting are shown in Table S3, 4. The first peak represents the Mn-O coordination shell and the

second peak is attributed to the Mn-TM (TM represents Mn or Cu) coordination shell. The corresponding fitting parameters for Mn-O and Mn-TM coordination shells are shown in Figure 5c-f.

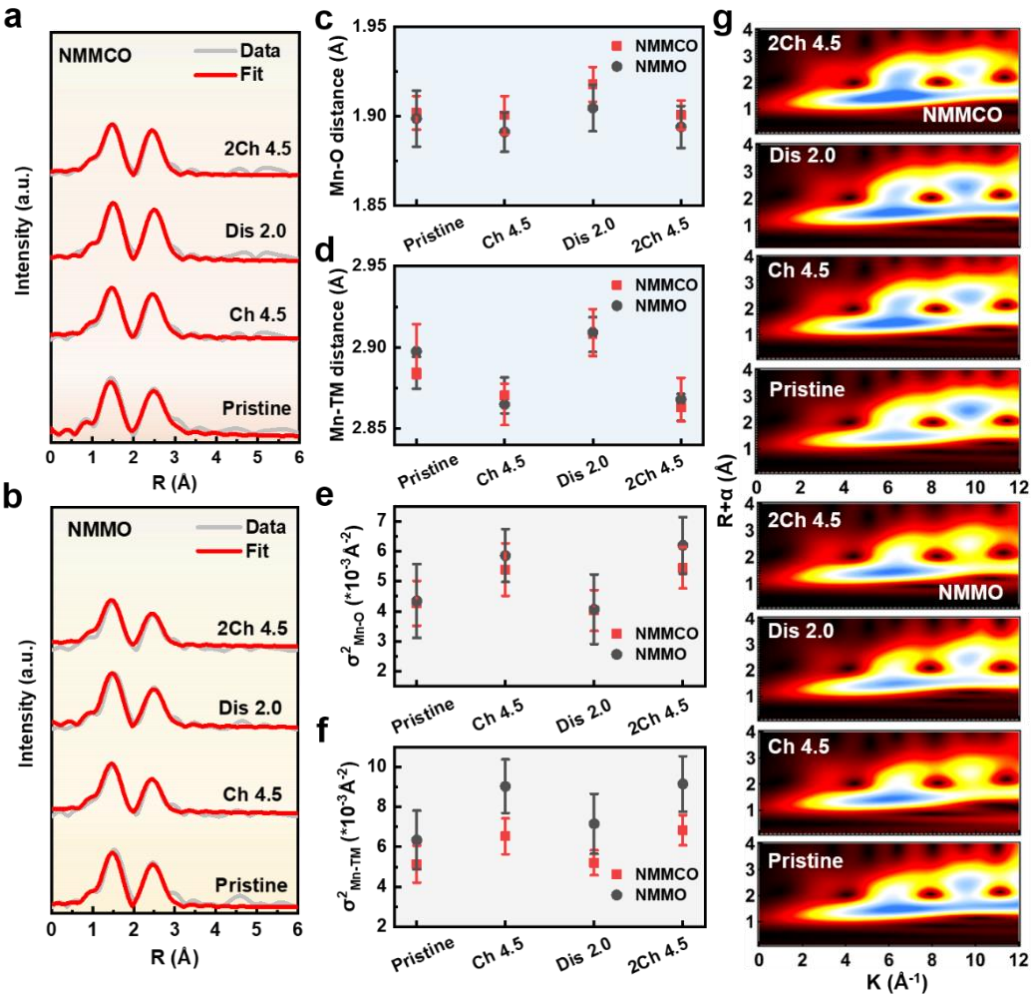

Figure 5. Mn K-edge FT-EXAFS spectra of (a) NMMCO and (b) NMMO at different states of charge. (c) Mn-O bond distance and (d) Mn-TM bond distance of NMMCO and NMMO. The Debye-Waller factor σ^2 of (e) Mn-O bond and (f) Mn-TM bond of NMMCO and NMMO. (g) WT-EXAFS spectra of NMMCO and NMMO at different states of charge.

The Mn-O bond distances of both cathodes at pristine state are very similar (Figure 5c), indicating the similar oxidation state of Mn in NMMCO and NMMO. However, the Mn-TM bond distance of NMMCO (2.885 Å) is shorter than that of NMMO (2.898 Å) (Figure 5d), which should be related

to the different arrangement of TMs in the two materials.[19] Upon removal of Na-ion, the Mn-O bond length slightly decreases to 1.900 Å and 1.891 Å for NMMCO and NMMO, respectively, as a consequence of the oxidation of Cu and O. In contrast, a clear decrease of the Mn-TM bond length to 2.870 Å for NMMCO and 2.865 Å for NMMO is observed, which can be well understood by considering the fact that the TM-TM bond distance is strongly influenced by the TM-O bond distance owing to the edge-shared octahedral structure.[53] Similarly, because of the reduction reaction of TM and O upon Na-ion insertion, the Mn-O (Mn-TM) bond length increases to 1.918 Å and 1.905 Å (2.908 Å and 2.909 Å) for NMMCO and NMMO in the following discharge process, respectively. The difference in Mn-O bond length after discharging should be related to the different lattice OR reversibility of NMMCO and NMMO. Note that similar TM-O and Mn-TM bond length evolution is also observed for the second charge process of both cathodes.

The Debye-Waller factor σ^2, which is closely related to the local structural disorder, is further discussed to get insight into the local environment associated with TM and O framwork.[54] The value of σ^2 of Mn-O octahedron increases from 4.27×10^{-3} to 5.39×10^{-3} for NMMCO and from 4.34×10^{-3} to 5.85×10^{-3} for NMMO (Figure 5e), suggesting more distortion of MnO_6 framework in NMMO. This is due to the largely irreversible lattice OR reactions in NMMO that destroys the rigid oxygen sublattice during Na-ion deintercalation. The value of σ^2 is further increased to 6.19×10^{-3} for NMMO after the second charge due to the accumulated structural distortion, while it basically maintains the same value of the first charge for NMMCO as a consequence of the well-maintained lattice rigidity due to the highly reversible OR reactions upon cycling. For the Mn-TM coordination shell, the increase of σ^2 for NMMCO (from 5.14×10^{-3} to 6.53×10^{-3}) is less significant compared to that for NMMO (from 6.34×10^{-3} to 9.03×10^{-3}) after the first charge (Figure 5f). Moreover, the σ^2

value of Mn-TM bond for NMMCO (5.20×10^{-3}) mostly recovers to its initial value (5.14×10^{-3}) upon following discharge, whereas the value for NMMO (7.15×10^{-3}) is considerably larger than its initial value (6.34×10^{-3}). Similar σ^2 value evolution is also observed for the second charge process. It has been observed that the migration of TM from TMO_2 layer to Na layer increases the σ^2 value of Mn-TM bond as a result of structural distortions.[55, 56] Therefore, the large and irreversible variation of σ^2 value of Mn-TM bond for NMMO upon cycling strongly suggests the largely irreversible TM migration through oxygen vacancies induced by lattice oxygen release.[57] In contrast, the highly reversible σ^2 value evolution for NMMCO indicates the high reversibility of TM migration during the Na-ion intercalation/extraction process, which should be related to the high covalency between Cu 3d and O 2p states that enables the strong lattice stiffness.

To supplement the EXAFS fitting results, wavelet transform (WT) analysis of Mn K-edge spectra is further performed to explore more intuitive changes of the surrounding coordination environments of TM (Figure 5g).[58] According to the WT contour plots, the scattering peaks located at (6.0 $Å^{-1}$, 1.5 Å) and (9.5 $Å^{-1}$, 2.5 Å) are attributed to the contributions of Mn-O and Mn-TM features, respectively, and the peak intensities are closely related to the evolution of local coordination environments, such as TM migration.[56, 58] During charging, the intensity of Mn-TM feature for NMMO is greatly reduced while it only slightly decrease for NMMCO. In the following discharge process, the intensity is only partially recovered for NMMO. In contrast, it almost fully goes back to the original state for NMMCO, which is also observed for the second cycle. These results, together with EXAFS analysis, imply that NMMO undergoes progressive local structural variations involving irreversible TM migration whereas NMMCO demonstrates suppressed and reversible TM migration. It is noteworthy that the unhybridized oxygen state could be the driving

force for TM migration according to the TM migration-oxygen redox coupling theory.[51] For NMMO possessing more nonbonding O 2p orbitals as a consequence of Na-O-Mg/vacancy configuration, it exhibits stronger TM migration compared to NMMCO. Moreover, the drastic change of local oxygen coordination environments due to the highly irreversible lattice OR reaction also facilitates the irreversible TM migration in NMMO.[59] On the contrary, the effective modulation of the covalency between O 2p and Cu 3d states and the enhanced reversibility of lattice OR can stabilize the framework structure of NMMCO, further leading to the improved TM migration reversibility.

The local structural evolution induced by distinct lattice OR reversibility of NMMO and NMMCO is also corroborated by the pre-edge features of Mn K-edge XANES spectra, which can distinguish the distortion of TMO_6 octahedral symmetry due to their sensitivity to local centrosymmetry.[60] The well-resolved pre-edge features at 6541 and 6543 eV of NMMO and NMMCO are shown in Figure S9, with the low-energy feature representing the transition from 1s to e_g states and the high-energy feature corresponding to the transition from 1s to t_{2g} states. Specifically, the pre-edge intensity of NMMO is increased by 1.5 times compared to that of NMMCO upon charging, suggesting the existence of more severe local lattice structural distortion. After discharge, the pre-edge features of NMMCO are fully recovered to the pristine state, while it is not the case for NMMO. This strongly implies the highly reversible structural evolution of NMMCO over cycling, which is in good accordance with the results discussed above. Moreover, the HRTEM images collected for electrodes after 20 cycles (Figure S10) suggest the more severe distortion of crystal planes of NMMO. Overall, by combining in-situ XRD, ex-situ EXAFS, and ex-situ mRIXS results, we unambiguously reveal that modulating TM-O covalency of layered battery electrodes can greatly enhance the reversibility of lattice OR reactions and concurrently suppress

the phase transition and irreversible TM migration, thus leading to the improved structural stability and electrochemical performance.

Finally, density of states (DOS) calculations were performed to shed light on the influence of Cu dopants on the lattice OR reversibility and structural stability (Figure 6). The DOS of NMMO (Figure 6a) shows more isolated O 2p states near the Fermi level. According to the schematic diagram of crystal structure of NMMO (Figure 6b), two different configurations of Mg-O-Na/vacancy and Mn-O-Na/vacancy exist in NMMO. Specifically, for Mg-O-Na/vacancy configuration, nonbonding O 2p states with elevated energy level toward Fermi level can be formed due to the energy difference between Mg/Na 3s and O 2p states (Figure 6e), which are similar to that in Li-rich materials.[11] The elevated nonbonding O 2p states are more facile to be oxidized at lower voltage region but with a less rigid TM-O framework in desodiated state, leading to a less reversible OR reaction and TM migration.[61, 62]

In contrast, one more configuration of Cu-O-Na/vacancy exists in NMMCO (Figure 6d). Both Cu 3d and O 2p states are dominated near the Fermi level for NMMCO (Figure 6c and f). The high energetic overlap between Cu 3d and O 2p states implies the presence of strong Cu-O covalency, in contrast to that of NMMO with the orphaned oxygen 2p band pinned at the highest occupied states (Figure 6e). Such strong Cu-O covalency creates more delocalized TM-O bonds to harden the oxygen lattice, resulting in more stable oxidized oxygen intermediates, thus improving the reversibility of lattice OR.[63]

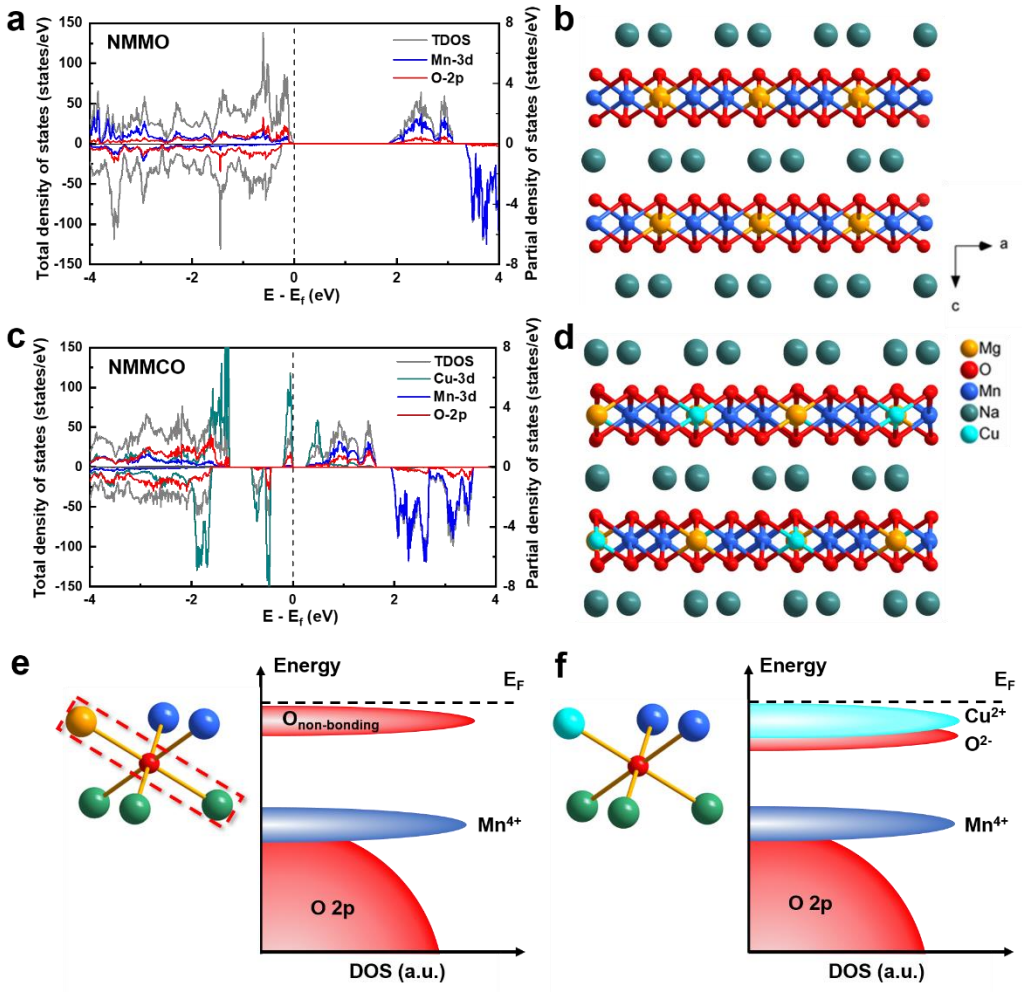

Figure 6. DOS calculation for (a) NMMO and (c) NMMCO at the pristine state. Schematic diagram of crystal structure at the [002] direction for (b) NMMO and (d) NMMCO. Schematic diagram of DOS for (e) NMMO and (f) NMMCO.

In the previous section, we have concluded that the distortion of TMO_2 octahedron is more serious for NMMO during the cycling process. From DOS calculations, we further suggest that the nonbonding oxygen 2p states may rotate upon Na-ion removal with a higher tendency to form O-O dimers and possibly trapped O_2 molecules due to less-directional TM-O bonding, resulting in aggravated local distortion.[11, 64] In contrast, the large energetic overlap of TM-O in NMMCO increases the overall energy barrier to rotate the O bonds, resulting in a more rigid oxygen lattice to improve the lattice OR reversibility and reduce the local disorder of MO_6 octahedron.

Conclusions

In summary, we have demonstrated that the reversibility of lattice OR reactions of layered battery electrodes can be greatly influenced by TM-O covalency. By partially substituting low-electronegativity Mg^{2+} with high-electronegativity Cu^{2+}, the reversibility of lattice OR reactions could be greatly improved from 73% for NMMO to 95% for NMMCO as a consequence of enhanced Cu-O covalency, which enables a more rigid oxygen lattice and less distorted TMO_6 octahedron upon Na-ion extraction/insertion. The enhanced lattice OR reversibility can also facilitate the reversible TM migration over cycling. In addition, the Cu dopants suppress the undesired "P2-OP4" phase transition and lead to a completely solid-solution behavior with an ultra-low volume variation of 0.45%, and therefore, NMMCO can be defined as a new zero-strain cathode material. Because of these advantages, NMMCO demonstrates a suppressed voltage fade and an improved capacity retention of 95.8% after 200 cycles at a high current rate of 1 C. Our present work highlights the significance of enhancing the lattice OR reversibility through modulation of TM-O covalency rather than just activating the oxygen oxidation activity by construction of overwhelming nonbonding oxygen states, which provides a guidance for future high-throughput screening of high-energy-density cathode materials utilizing OR chemistry.

Acknowledgements

This work is supported by the National Natural Science Foundation of China (11905154), the Natural Science Foundation of the Jiangsu Higher Education Institutions of China (19KJA550004), the Natural Science Foundation of Jiangsu Province (BK20190814), Collaborative Innovation Center of Suzhou Nano Science & Technology, Suzhou Key Laboratory of Functional Nano & Soft Materials, the 111 Project, Soochow University-Western University Centre for Synchrotron Radiation Research. The work at Advanced Light Source of the Lawrence Berkeley National

Laboratory is supported by the Director, Office of Science, Office of Basic Energy Sciences, of the U.S. Department of Energy under Contract No. DE-AC02-05CH11231. The authors thank SSRF (beamline 02B02 and 11B), TLS (beamline 20A), ALS (beamline 8.0.1), NSRL (beamline 11U), and BSRF (beamline 1W1B) for the allocation of synchrotron beamtime.

Reference

1. Armand, M.; Tarascon, J. M. *Nature* **2008,** 451, (7179), 652-657.

2. Goodenough, J. B.; Kim, Y. *Chem. Mater.* **2010,** 22, (3), 587-603.

3. Assat, G.; Tarascon, J.-M. *Nat. Energy* **2018,** 3, (5), 373-386.

4. Li, B.; Xia, D. *Adv. Mater.* **2017,** 29, (48), 1701054.

5. Myeong, S.; Cho, W.; Jin, W.; Hwang, J.; Yoon, M.; Yoo, Y.; Nam, G.; Jang, H.; Han, J.-G.; Choi, N.-S.; Kim, M. G.; Cho, J. *Nat. Commun.* **2018,** 9, (1), 3285.

6. Rahman, M. M.; Lin, F. *Matter* **2021,** 4, (2), 490-527.

7. Yang, W. *Nat. Energy* **2018,** 3, (8), 619-620.

8. Wu, J.; Zhuo, Z.; Rong, X.; Dai, K.; Lebens-Higgins, Z.; Sallis, S.; Pan, F.; Piper Louis, F. J.; Liu, G.; Chuang, Y.-d.; Hussain, Z.; Li, Q.; Zeng, R.; Shen, Z.-x.; Yang, W. *Sci. Adv.* 6, (6), eaaw3871.

9. Cheng, C.; Li, S.; Liu, T.; Xia, Y.; Chang, L.-Y.; Yan, Y.; Ding, M.; Hu, Y.; Wu, J.; Guo, J.; Zhang, L. *ACS Appl. Mater. Interfaces* **2019,** 11, (44), 41304-41312.

10. Li, M.; Bi, X.; Amine, K.; Lu, J. *Acc. Chem. Res.* **2020,** 53, (8), 1436-1444.

11. Seo, D. H.; Lee, J.; Urban, A.; Malik, R.; Kang, S.; Ceder, G. *Nat. Chem.* **2016,** 8, (7), 692-7.

12. Zhang, J.; Cheng, F.; Chou, S.; Wang, J.; Gu, L.; Wang, H.; Yoshikawa, H.; Lu, Y.; Chen, J. *Adv. Mater.* **2019,** 31, (42), 1901808.

13. Zhao, C.; Wang, Q.; Lu, Y.; Jiang, L.; Liu, L.; Yu, X.; Chen, L.; Li, B.; Hu, Y.-S. *Energy Stor. Mater.* **2019,** 20, 395-400.

14. Ben Yahia, M.; Vergnet, J.; Saubanère, M.; Doublet, M.-L. *Nat. Mater.* **2019,** 18, (5), 496-502.

15. Sathiya, M.; Rousse, G.; Ramesha, K.; Laisa, C. P.; Vezin, H.; Sougrati, M. T.; Doublet, M. L.; Foix, D.; Gonbeau, D.; Walker, W.; Prakash, A. S.; Ben Hassine, M.; Dupont, L.; Tarascon, J. M. *Nat. Mater.* **2013,** 12, (9), 827-835.

16. Li, Q.; Zhou, D.; Zhang, L.; Ning, D.; Chen, Z.; Xu, Z.; Gao, R.; Liu, X.; Xie, D.; Schumacher, G.; Liu, X. *Adv. Funct. Mater.* **2019,** 29, (10), 1806706.

17. Dai, K.; Wu, J.; Zhuo, Z.; Li, Q.; Sallis, S.; Mao, J.; Ai, G.; Sun, C.; Li, Z.; Gent, W. E.; Chueh, W. C.; Chuang, Y.-d.; Zeng, R.; Shen, Z.-x.; Pan, F.; Yan, S.; Piper, L. F. J.; Hussain, Z.; Liu, G.; Yang, W. *Joule* **2019,** 3, (2), 518-541.

18. Yabuuchi, N.; Hara, R.; Kajiyama, M.; Kubota, K.; Ishigaki, T.; Hoshikawa, A.; Komaba, S. *Adv. Energy Mater.* **2014,** 4, (13), 1301453.

19. Zhang, L.; Wang, J.; Schuck, G.; Xi, F.; Du, L.; Winter, M.; Schumacher, G.; Li, J. *Small Methods* **2020,** 4, (10), 2000422.

20. Cheng, C.; Ding, M.; Yan, T.; Dai, K.; Mao, J.; Zhang, N.; Zhang, L.; Guo, J. *Energies* **2020,** 13, (21), 5729.

21. Ku, K.; Hong, J.; Kim, H.; Park, H.; Seong, W. M.; Jung, S.-K.; Yoon, G.; Park, K.-Y.; Kim, H.; Kang, K. *Adv. Energy Mater.* **2018,** 8, (21), 1800606.

22. Konarov, A.; Kim, H. J.; Jo, J.-H.; Voronina, N.; Lee, Y.; Bakenov, Z.; Kim, J.; Myung, S.-T. *Adv. Energy Mater.* **2020,** 10, (24), 2001111.

23. Wang, P.-F.; Yao, H.-R.; Liu, X.-Y.; Yin, Y.-X.; Zhang, J.-N.; Wen, Y.; Yu, X.; Gu, L.; Guo, Y.-

G. *Sci. Adv.* 4, (3), eaar6018.

24. Liu, X.; Zuo, W.; Zheng, B.; Xiang, Y.; Zhou, K.; Xiao, Z.; Shan, P.; Shi, J.; Li, Q.; Zhong, G.; Fu, R.; Yang, Y. *Angew. Chem. Int. Ed.* **2019,** 58, (50), 18086-18095.

25. Zheng, W.; Liu, Q.; Wang, Z.; Wu, Z.; Gu, S.; Cao, L.; Zhang, K.; Fransaer, J.; Lu, Z. *Energy Stor. Mater.* **2020,** 28, 300-306.

26. Bai, X.; Sathiya, M.; Mendoza-Sánchez, B.; Iadecola, A.; Vergnet, J.; Dedryvère, R.; Saubanère, M.; Abakumov, A. M.; Rozier, P.; Tarascon, J.-M. *Adv. Energy Mater.* **2018,** 8, (32), 1802379.

27. Wang, K.; Wan, H.; Yan, P.; Chen, X.; Fu, J.; Liu, Z.; Deng, H.; Gao, F.; Sui, M. *Adv. Mater.* **2019,** 31, (46), 1904816.

28. Park, Y. J.; Choi, J. U.; Jo, J. H.; Jo, C.-H.; Kim, J.; Myung, S.-T. *Adv. Funct. Mater.* **2019,** 29, (28), 1901912.

29. Xu, H.; Cheng, C.; Chu, S.; Zhang, X.; Wu, J.; Zhang, L.; Guo, S.; Zhou, H. *Adv. Funct. Mater.* **2020,** 30, (50), 2005164.

30. Kim, H. J.; Konarov, A.; Jo, J. H.; Choi, J. U.; Ihm, K.; Lee, H.-K.; Kim, J.; Myung, S.-T. *Adv. Energy Mater.* **2019,** 9, (32), 1901181.

31. Zhang, X.; Qiu, F.; Jiang, K.; He, P.; Han, M.; Guo, S.; Zhou, H. *Chem. Commun.* **2020,** 56, (46), 6293-6296.

32. Yang, L.; Li, X.; Liu, J.; Xiong, S.; Ma, X.; Liu, P.; Bai, J.; Xu, W.; Tang, Y.; Hu, Y.-Y.; Liu, M.; Chen, H. *J. Am. Chem. Soc.* **2019,** 141, (16), 6680-6689.

33. Liu, Y.; Wang, C.; Zhao, S.; Zhang, L.; Zhang, K.; Li, F.; Chen, J. *Chem. Sci.* **2021,** 12, (3), 1062-1067.

34. Jin, T.; Wang, P.-F.; Wang, Q.-C.; Zhu, K.; Deng, T.; Zhang, J.; Zhang, W.; Yang, X.-Q.; Jiao, L.; Wang, C. *Angew. Chem. Int. Ed.* **2020,** 59, (34), 14511-14516.

35. Wang, C.; Liu, L.; Zhao, S.; Liu, Y.; Yang, Y.; Yu, H.; Lee, S.; Lee, G.-H.; Kang, Y.-M.; Liu, R.; Li, F.; Chen, J. *Nat. Commun.* **2021,** 12, (1), 2256.

36. Liu, Z.; Shen, J.; Feng, S.; Huang, Y.; Wu, D.; Li, F.; Zhu, Y.; Gu, M.; Liu, Q.; Liu, J.; Zhu, M. *Angew. Chem. Int. Ed.* **2021,** 60, (38), 20960-20969.

37. Wang, Y.; Wang, L.; Zhu, H.; Chu, J.; Fang, Y.; Wu, L.; Huang, L.; Ren, Y.; Sun, C.-J.; Liu, Q.; Ai, X.; Yang, H.; Cao, Y. *Adv. Funct. Mater.* **2020,** 30, (13), 1910327.

38. Lu, Z.; Dahn, J. R. *J. Electrochem. Soc.* **2001,** 148, (11), A1225.

39. Tarascon, J.-M. *Joule* **2020,** 4, (8), 1616-1620.

40. Billaud, J.; Singh, G.; Armstrong, A. R.; Gonzalo, E.; Roddatis, V.; Armand, M.; Rojo, T.; Bruce, P. G. *Energy Environ. Sci.* **2014,** 7, (4), 1387-1391.

41. Zuo, W.; Liu, X.; Qiu, J.; Zhang, D.; Xiao, Z.; Xie, J.; Ren, F.; Wang, J.; Li, Y.; Ortiz, G. F.; Wen, W.; Wu, S.; Wang, M.-S.; Fu, R.; Yang, Y. *Nat. Commun.* **2021,** 12, (1), 4903.

42. Hu, E.; Yu, X.; Lin, R.; Bi, X.; Lu, J.; Bak, S.; Nam, K.-W.; Xin, H. L.; Jaye, C.; Fischer, D. A.; Amine, K.; Yang, X.-Q. *Nat. Energy* **2018,** 3, (8), 690-698.

43. Achkar, A. J.; Regier, T. Z.; Wadati, H.; Kim, Y. J.; Zhang, H.; Hawthorn, D. G. *Phys. Rev. B* **2011,** 83, (8), 081106.

44. Eisebitt, S.; Böske, T.; Rubensson, J. E.; Eberhardt, W. *Phys. Rev. B* **1993,** 47, (21), 14103-14109.

45. Yang, W.; Devereaux, T. P. *J. Power Sources* **2018,** 389, 188-197.

46. Li, X.-L.; Wang, T.; Yuan, Y.; Yue, X.-Y.; Wang, Q.-C.; Wang, J.-Y.; Zhong, J.; Lin, R.-Q.; Yao,

Y.; Wu, X.-J.; Yu, X.-Q.; Fu, Z.-W.; Xia, Y.-Y.; Yang, X.-Q.; Liu, T.; Amine, K.; Shadike, Z.; Zhou, Y.-N.; Lu, J. *Adv. Mater.* **2021,** 33, (13), 2008194.

47. Wu, J.; Li, Q.; Sallis, S.; Zhuo, Z.; Gent, W. E.; Chueh, W. C.; Yan, S.; Chuang, Y.-d.; Yang, W. *Condens. Matter* **2019,** 4, (1).

48. de Groot, F. M. F.; Grioni, M.; Fuggle, J. C.; Ghijsen, J.; Sawatzky, G. A.; Petersen, H. *Phys. Rev. B* **1989,** 40, (8), 5715-5723.

49. Zhou, K.; Zheng, S.; Ren, F.; Wu, J.; Liu, H.; Luo, M.; Liu, X.; Xiang, Y.; Zhang, C.; Yang, W.; He, L.; Yang, Y. *Energy Stor. Mater.* **2020,** 32, 234-243.

50. Chen, D.; Wu, J.; Papp, J. K.; McCloskey, B. D.; Yang, W.; Chen, G. *Small* **2020,** 16, (22), 2000656.

51. Lee, G.-H.; Lau, V. W.-h.; Yang, W.; Kang, Y.-M. *Adv. Energy Mater.* **2021,** 11, (27), 2003227.

52. Hong, J.; Gent, W. E.; Xiao, P.; Lim, K.; Seo, D.-H.; Wu, J.; Csernica, P. M.; Takacs, C. J.; Nordlund, D.; Sun, C.-J.; Stone, K. H.; Passarello, D.; Yang, W.; Prendergast, D.; Ceder, G.; Toney, M. F.; Chueh, W. C. *Nat. Mater.* **2019,** 18, (3), 256-265.

53. Lee, G.-H.; Wu, J.; Kim, D.; Cho, K.; Cho, M.; Yang, W.; Kang, Y.-M. *Angew. Chem. Int. Ed.* **2020,** 59, (22), 8681-8688.

54. Karan, N. K.; Slater, M. D.; Dogan, F.; Kim, D.; Johnson, C. S.; Balasubramanian, M. *J. Electrochem. Soc.* **2014,** 161, (6), A1107-A1115.

55. Hirsh, H.; Li, Y.; Cheng, J.-H.; Shimizu, R.; Zhang, M.; Zhao, E.; Meng, Y. S. *J. Electrochem. Soc.* **2021,** 168, (4), 040539.

56. Yin, C.; Wan, L.; Qiu, B.; Wang, F.; Jiang, W.; Cui, H.; Bai, J.; Ehrlich, S.; Wei, Z.; Liu, Z. *Energy Stor. Mater.* **2021,** 35, 388-399.

57. Kong, W.; Zhang, J.; Wong, D.; Yang, W.; Yang, J.; schulze, c.; Liu, X. *Angew. Chem. Int. Ed.* **2021,** n/a, (n/a).

58. Martini, A.; Signorile, M.; Negri, C.; Kvande, K.; Lomachenko, K. A.; Svelle, S.; Beato, P.; Berlier, G.; Borfecchia, E.; Bordiga, S. *PCCP* **2020,** 22, (34), 18950-18963.

59. Gent, W. E.; Lim, K.; Liang, Y.; Li, Q.; Barnes, T.; Ahn, S.-J.; Stone, K. H.; McIntire, M.; Hong, J.; Song, J. H.; Li, Y.; Mehta, A.; Ermon, S.; Tyliszczak, T.; Kilcoyne, D.; Vine, D.; Park, J.-H.; Doo, S.-K.; Toney, M. F.; Yang, W.; Prendergast, D.; Chueh, W. C. *Nat. Commun.* **2017,** 8, (1), 2091.

60. Talaie, E.; Kim, S. Y.; Chen, N.; Nazar, L. F. *Chem. Mater.* **2017,** 29, (16), 6684-6697.

61. Yu, Y.; Karayaylali, P.; Nowak, S. H.; Giordano, L.; Gauthier, M.; Hong, W.; Kou, R.; Li, Q.; Vinson, J.; Kroll, T.; Sokaras, D.; Sun, C.-J.; Charles, N.; Maglia, F.; Jung, R.; Shao-Horn, Y. *Chem. Mater.* **2019,** 31, (19), 7864-7876.

62. Charles, N.; Yu, Y.; Giordano, L.; Jung, R.; Maglia, F.; Shao-Horn, Y. *Chem. Mater.* **2020,** 32, (13), 5502-5514.

63. Cao, X.; Li, H.; Qiao, Y.; Li, X.; Jia, M.; Cabana, J.; Zhou, H. *Adv. Energy Mater.* **2020,** 10, (15), 1903785.

64. Boivin, E.; House, R. A.; Pérez-Osorio, M. A.; Marie, J.-J.; Maitra, U.; Rees, G. J.; Bruce, P. G. *Joule* **2021,** 5, (5), 1267-1280.

TOC

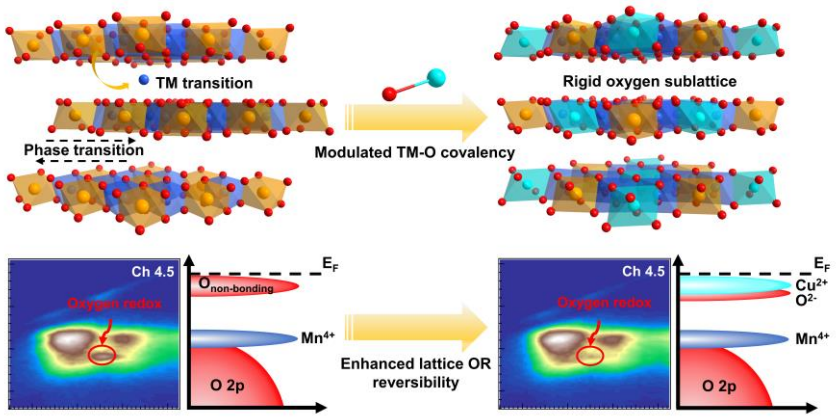

Instead of activating the oxygen oxidation activity by construction of overwhelming nonbonding oxygen states, it is more crucial to enhance the reversibility of lattice oxygen redox reactions of layered battery electrodes through modulating transition metal (TM)-O covalency, which concurrently suppresses the phase transition and irreversible TM migration, thus leading to the improved structural stability and electrochemical performance.